metals

MDPI

Article

Microstructure and Oxidation Behavior of Carbide-Metal Cermet Material with Hybrid Binder

Yunyi Zhu [1], Yi Xie [1], Wei Wang [2,3], Juanqiang Ding [2,3], Zhixing Guo [4,*], Longgang Wang [4], Xiang Xia [4], Guang Xian [4], Tianen Yang [4], Jinwen Cai [4] and Mei Yang [1,*]

[1] College of Materials and Chemistry & Chemical Engineering, Chengdu University of Technology, Chengdu 610059, China; m15808204277@163.com (Y.Z.); xieyi202512@163.com (Y.X.)
[2] State Key Laboratory of Clean and Efficient Turbomachinery Power Equipment, Deyang 618000, China
[3] Dongfang Electric Corporation Dongfang Turbine Co., Ltd., Deyang 618000, China
[4] School of Mechanical Engineering, Sichuan University, Chengdu 610065, China
* Correspondence: guozhixing@scu.edu.cn (Z.G.); yangmei09@cdut.edu.cn (M.Y.)

Abstract

To address the limitations of cobalt-based cermet in oxidative and high-temperature environments, this study investigates a (W,Ti)C-based cermet system incorporating a hybrid binder composed of nickel (Ni) and 304 stainless steel (304ss). A series of cermets with varying Ni/304ss binder metal ratios were fabricated via vacuum sintering at 1440 °C. The introduction of 304ss into the Ni matrix enhanced interfacial diffusion and phase stability, effectively suppressing core–rim structures and promoting a uniform microstructure. Notably, the cermet with 8%Ni–8%304ss composition achieved a Vickers hardness of 15.6 GPa and fracture toughness of 9.21 MPa·m$^{1/2}$, balancing mechanical strength and toughness. Isothermal oxidation testing at 450 °C showed that the hybrid binder substantially suppressed specific mass gain compared to monolithic Ni or 304ss systems. These improvements are attributed to the interplay between Ni-enhanced densification, which limits oxygen transport, and Cr-facilitated surface passivation, which stabilizes the oxide layer. The results highlight the potential of Ni-304ss hybrid binders as cobalt-free alternatives for high-performance tooling and wear-resistant applications in oxidative environments.

Keywords: cermet; (W,Ti)C; hybrid binder; oxidation resistance

1. Introduction

Cermets, which integrate hard ceramic phases with ductile metallic binders, remain indispensable for cutting tools, mining bits, and wear components due to their exceptional hardness, toughness, and thermal stability [1–4]. Since the 1920s, WC-Co composites have dominated the cemented carbide market because cobalt provides excellent wetting of WC particles and effective toughening [5]. However, the inherent limitations of cobalt-based systems, particularly their susceptibility to oxidation-induced degradation, have become a critical barrier to performance in high-temperature applications. At temperatures above 400 °C, WC-Co cermets form non-protective NiO and CoO scales during machining and drilling operations [6,7], leading to accelerated material loss and significantly reduced service life in oxidative environments [8]. This oxidation behavior, coupled with the relatively low hardness of cobalt-bonded materials compared to alternative binders, has intensified the demand for cobalt-free solutions with enhanced thermal stability.

Check for updates

Academic Editor: Eric Hug

Received: 29 December 2025
Revised: 3 February 2026
Accepted: 5 February 2026
Published: 9 February 2026

Copyright: © 2026 by the authors. Licensee MDPI, Basel, Switzerland. This article is an open access article distributed under the terms and conditions of the Creative Commons Attribution (CC BY) license.

Recent strategies for cobalt-free cermet development focus on two approaches: (i) modification of the carbide phase and (ii) advanced binder engineering. For the carbide phase, (W,Ti)C solid solutions have emerged as promising candidates due to Ti substitution that stabilizes the cubic NaCl-type structure, suppresses η-phase formation, and improves high-temperature oxidation resistance compared to pure WC [9–11]. Thermodynamic modeling confirms that Ti substitution delays oxidation onset by approximately 100–200 °C through Gibbs free energy stabilization, making (W,Ti)C particularly suitable for thermal cycling and oxidative environments [12,13].

In binder engineering, nickel has been extensively studied as a cobalt substitute due to its low cost, acceptable toughness, and excellent wettability with carbides (contact angles < 10°) [14]. However, Ni-bonded cermets typically exhibit 10–20% lower hardness than cobalt-based counterparts, and their NiO scales become porous above 400 °C, accelerating degradation in oxidative conditions [15,16]. In contrast, 304 stainless steel (Fe-18Cr-8Ni) binders form protective Cr_2O_3 layers that reduce parabolic oxidation rates by up to 50% at 600 °C [17,18]. Pure 304ss binders, however, face challenges including poor wettability with carbides, thermal expansion coefficient mismatches (~5×10^{-6} K^{-1}), and sensitization-induced intergranular embrittlement from Cr-depletion zones (1–5 μm width) [19].

Hybrid Ni-304ss binders combine the wettability advantages of nickel with the oxidation resistance of Cr in 304ss [20]. Nickel promotes microstructural refinement through dissolution–reprecipitation cycles, while Cr inhibits grain boundary weakening and forms compact oxide barriers via rapid Ni-Cr interdiffusion [21]. This strategy has demonstrated effectiveness in WC-TiC systems by suppressing core-rim structures and improving hardness–toughness balance. However, systematic studies on the impact of varying Ni/304ss ratios in (W,Ti)C matrices remain limited, particularly regarding core-rim suppression, porosity evolution, mechanical properties, and oxidation behavior at 400–500 °C [22,23]. Unlike previous studies focusing on complex high-entropy alloys or single-metal binders, this work systematically explores the synergy between Ni and 304ss to achieve a superior balance of toughness and oxidation resistance [24,25].

This study systematically investigates (W,Ti)C-based cermets with a hybrid binder composition of 16 wt.% (xNi + (16 − x)304ss) (x = 0, 4, 8, 12, 16) fabricated through vacuum sintering at 1440 °C. Comprehensive characterization of phase constitution, densification behavior, microstructural features, Vickers hardness, fracture toughness, and isothermal oxidation resistance at 450 °C is conducted. The work emphasizes the synergistic effects of Ni-enhanced wetting and Cr-derived passivation mechanisms. These findings establish a foundation for developing cobalt-free cermets tailored for demanding oxidative and tribological applications.

2. Experimental Procedures

2.1. Materials and Preparation

(W,Ti)C-Ni-304ss cermets were fabricated using powder metallurgy techniques. Commercially available (W,Ti)C powder (particle size ~2–5 μm, purity > 99.5%), Ni powder (particle size ~1–3 μm, purity > 99.9%), and 304 stainless steel (304ss) powder (particle size ~5–10 μm, composition: Fe-18Cr-8Ni, purity > 99%) were used as starting materials. The compositions were designed with a fixed total binder phase of 16 wt.% and varying Ni/304ss ratios, as detailed in Table 1.

Figure 1 provides a flowchart of the preparation process for (W,Ti)C-Ni-304ss cermet. The powders were accurately weighed according to Table 1 and mixed in anhydrous ethanol (99.9% purity) for 24 h using planetary ball milling to achieve homogeneous dispersion. The 24 h milling duration was selected to allow sufficient deagglomeration without inducing

excessive cold welding or contamination, as prolonged milling can introduce defects in ductile phases like Ni. WC-6Co cemented carbide balls (diameters: 6 mm and 10 mm, mass ratio 9:1) served as grinding media, with a ball-to-powder ratio of 10:1 and a rotational speed of 300 rpm. This ensures homogeneous mixing, reduces agglomeration, and promotes densification. The resulting slurry was sieved through a 400-mesh sieve to remove large aggregates and dried at 80 °C in a vacuum oven for 12 h to prevent oxidation.

Table 1. Composition of the (W,Ti)C-Ni-304ss cermets (wt.%).

Sample Number	(Ti,W)C (wt.%)	Ni (wt.%)	304 (wt.%)
A1	84	0	16
A2	84	4	12
A3	84	8	8
A4	84	12	4
A5	84	16	0

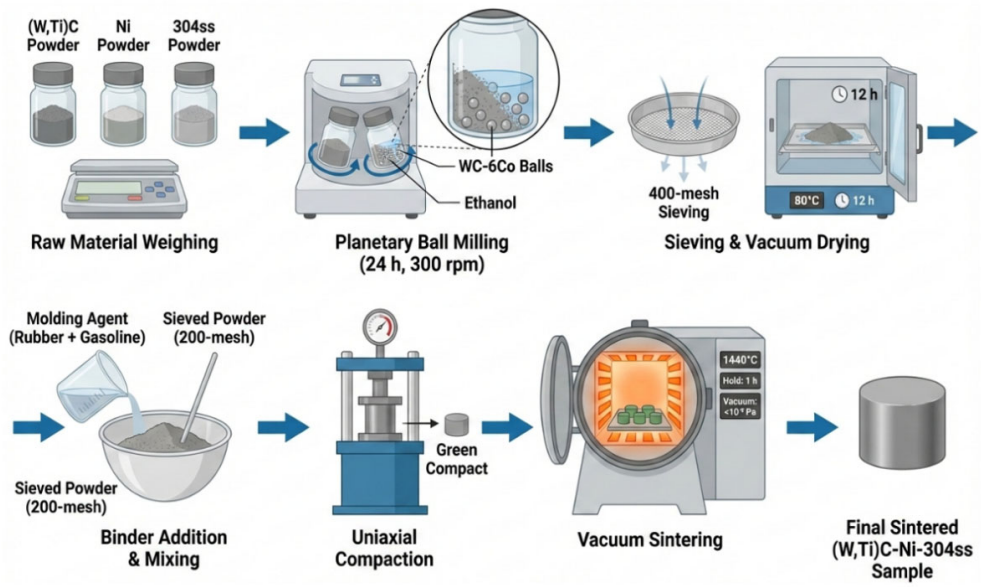

Figure 1. Flowchart of the preparation process for (W,Ti)C-Ni-304ss cermets.

After drying, the powder was sieved through a 200-mesh screen to control particle size distribution. A molding agent was prepared by dissolving synthetic rubber in gasoline at a 2:1 volume ratio, which acted as a temporary binder to enhance green compact strength. The agent was added to the sieved powder (typically 2–3 wt.% based on total mass) and thoroughly mixed. The mixture was then uniaxially in a cylindrical die (diameter ~10–15 mm, height ~5–10 mm) to form green compacts.

Figure 2 provides a Sintering curve diagram for (W,Ti)C-Ni-304ss cermet. Sintering was conducted in a vacuum furnace (<10^{-2} Pa) at 1440 °C with a heating rate of 10 °C/min and a holding time of 1 h, followed by furnace cooling to room temperature under vacuum. Although the optimal sintering windows for Ni and 304ss binders differ slightly, a unified temperature of 1440 °C was selected to eliminate thermal history as a variable, ensuring that property variations are solely attributable to binder composition. The sintering temperature was chosen to balance the liquid phase viscosity of the Ni-Cr-Fe alloy and the dissolution-reprecipitation rate of the carbide phase. Lower temperatures lead to residual porosity, while higher temperatures trigger rapid grain coarsening of the (W,Ti)C matrix [26,27]. The furnace cooling rate was approximately 5–10 °C/min.

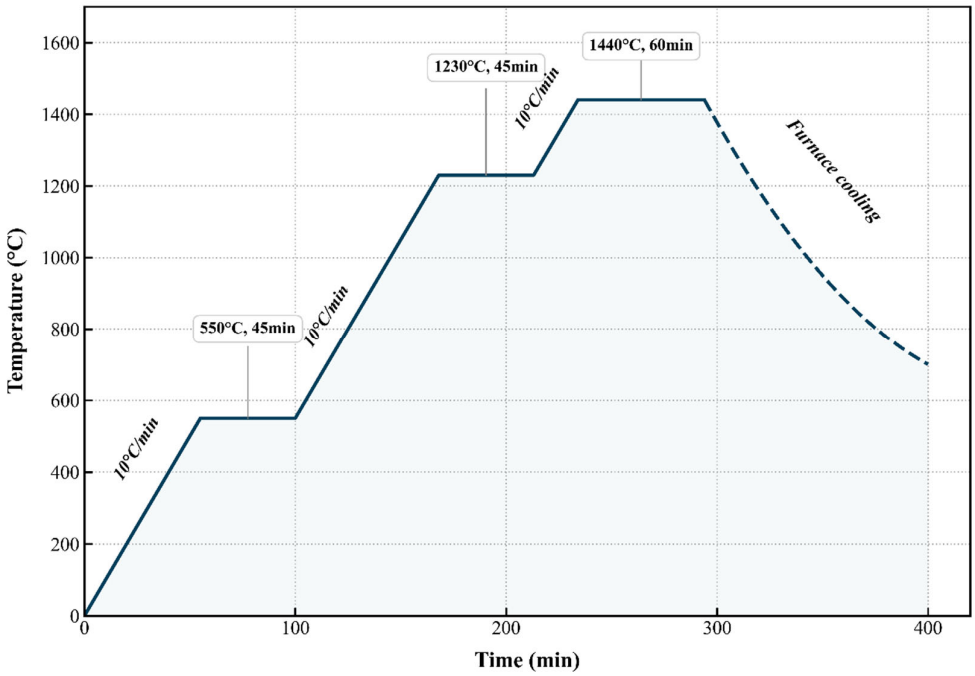

Figure 2. Sintering curve diagram.

2.2. Characterization

Sintered samples were ground and polished to a mirror finish using diamond abrasives (down to 1 μm) for microstructural analysis. Microstructures were examined using scanning electron microscopy (SEM) (Phenom ProX, Phenom, Shanghai, China) at an accelerating voltage of 15 kV, coupled with energy-dispersive X-ray spectroscopy (EDS) (DX-2700, Haoyuan, Dandong, China) for elemental mapping and point analysis.

Phase composition was determined by X-ray diffraction (XRD) using Cu Kα radiation (λ = 1.5406 Å), with an operating voltage of 40 kV, current of 30 mA, scanning range of 5–80° (2θ), step size of 0.02°, and scan speed of 0.02°/s. Peak identification was performed against standard PDF cards.

Density was measured via the Archimedes principle using a precision electronic balance. Theoretical density (ρ_0) was calculated using the rule of mixtures (Equation (1)):

$$\rho_0 = \frac{1}{\sum \frac{\omega_i}{\rho_i}} \quad (1)$$

where w_i is the weight fraction of component i, and ρ_i is its theoretical density (g/cm^3): (W,Ti)C ≈ 10.5 g/cm^3, Ni ≈ 8.9 g/cm^3, 304ss ≈ 7.9 g/cm^3. Relative density was obtained as (measured density/ρ_0) × 100%.

The Vickers Indentation Fracture (VIF) method was adopted as it constitutes the standard industrial protocol for the rapid and efficient screening of static toughness in cermet tool materials [27]. Vickers hardness (HV) was evaluated using a microhardness tester (HMAS-D1000SZ, Yanrun, Shanghai, China) at a load of 0.1 kg (0.981 N) and dwell time of 10 s, with at least 10 indentations per sample for statistical reliability.

Fracture toughness (K_{IC}) was assessed using the Vickers indentation method at a load of 30 kg (294.2 N), calculated via Equation (2):

$$K_{IC} = A \cdot HV \cdot \sqrt{\frac{P}{\sum l_i}} \quad (2)$$

where P is the applied load (kg), HV is the Vickers hardness at 30 kg (N/mm^2), l_i are the crack lengths from indentation corners (mm), and A is a constant (0.0028). The schematic diagram of the indentation method for fracture toughness testing is shown in Figure 3.

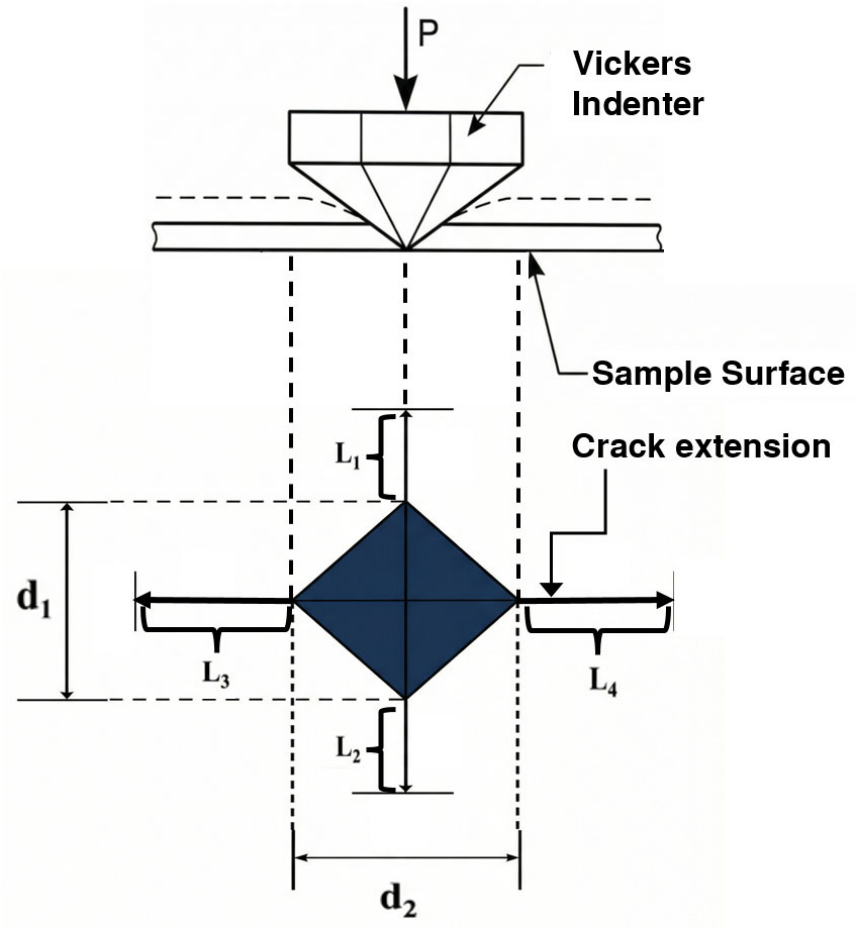

Figure 3. Schematic diagram of indentation method for fracture toughness testing.

Oxidation resistance was tested in a muffle furnace at 450 °C (heating rate: 5 °C/min, air atmosphere). Mass changes were recorded using a precision balance before and after oxidation to quantify mass gain due to oxide formation.

All characterizations were performed at room temperature unless specified, with samples sectioned perpendicular to the pressing direction for consistency. Statistical analysis (e.g., mean ± standard deviation) was applied to ensure data reliability.

3. Results and Discussion

3.1. Phase Analysis

Figure 4 presents the X-ray diffraction (XRD) patterns of (W,Ti)C-x wt.% 304ss-(16 − x) wt.% Ni cermets, where x = 0, 4, 8, 12, and 16. The diffraction results reveal distinct phase evolution as the binder composition varies. Across all samples, no reflections corresponding to W_2C or free carbon are observed, signifying that no decarburization occurred during sintering—a critical indicator of process stability and carbon retention [28,29]. All samples display prominent peaks located at approximately 2θ = 36.10°, 41.93°, 60.79°, 72.78°, and 76.59°, which correspond to the (111), (200), (220), (311), and (222) planes of the (W,Ti)C solid solution, in strong agreement with the standard reference PDF#03-065-8811. These peaks confirm that (W,Ti)C remains the dominant ceramic phase regardless of the binder system.

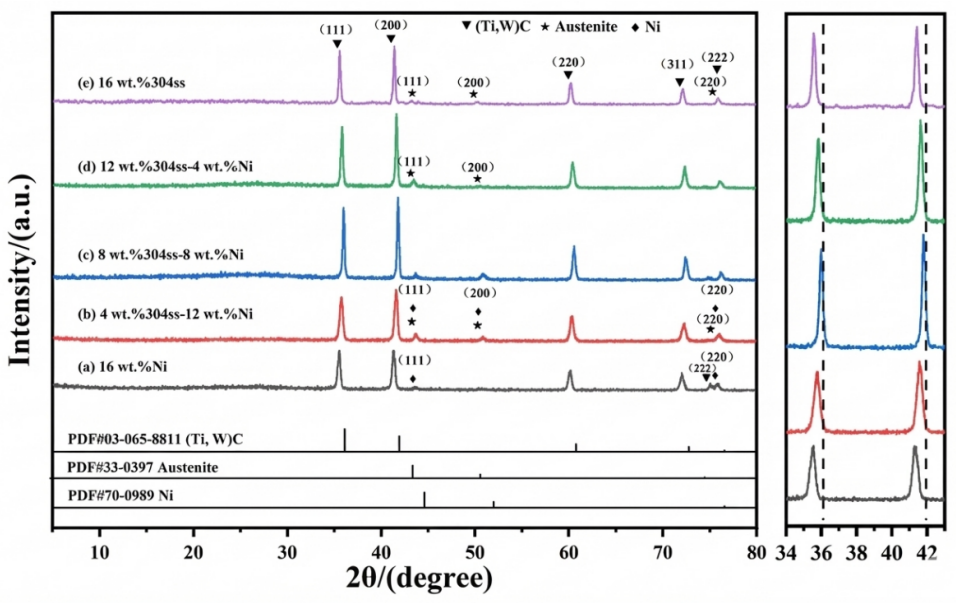

Figure 4. XRD of (W,Ti)C-x304ss-(16 − x)Ni (x = 0, 4, 8, 12, 16%) cermets.

When Ni is used as the sole binder (sample A1), clear reflections appear at 2θ = 43.58°, 50.79°, and 74.70°, attributable to the face-centered cubic (FCC) structure of elemental nickel (PDF#70-0989) [30]. In contrast, in the 304ss-only sample (sample A5), peaks are observed at 44.60°, 51.98°, and 76.59°, consistent with the austenitic phase of stainless steel (PDF#33-0397) [31]. Thermodynamically, the strong austenite-stabilizing effect of Ni in the Fe-Ni-Ti system inhibits brittle intermetallic precipitation by retaining Ti in solid solution. Notably, both Ni and austenite exhibit FCC structures with similar lattice planes—(111), (200), and (220)—giving rise to overlapping diffraction signals in mixed-binder samples (samples b–d). These superimposed peaks lead to enhanced reflection intensities in the corresponding regions, compared to samples with a single binder, thus indicating a combined contribution from both metallic phases [32]. A magnified view of the 2θ range between 34° and 43° reveals that the primary peaks of all samples shift towards higher 2θ angles, consistent with a decrease in interplanar spacing as described by Bragg's law. This shift indicates a reduction in the lattice parameter of the ceramic phase, serving as a sensitive indicator of structural evolution during binder substitution. The observed shift to higher angles suggests lattice contraction. This is likely attributed to the dissolution of binder elements (such as Cr and Fe) with smaller atomic radii into the (W,Ti)C lattice, which substitutes the larger Ti/W atoms and reduces the lattice parameter [33,34].

Importantly, the magnitude of the peak shift exhibits a non-linear relationship with binder composition. As 304ss content increases from 0 to 8 wt.%, the magnitude of the shift diminishes, reaching a minimum in the composition with 8 wt.% 304ss and 8 wt.% Ni (sample A3). Beyond this point, further substitution of Ni with 304ss causes the shift to re-intensify, indicating a renewed increase in lattice distortion. This behavior suggests that both Ni and 304ss are capable of partially mitigating lattice stress in the (W,Ti)C phase, likely through distinct solute–matrix interactions or mismatch accommodation during sintering. However, the combination of the two binders appears to produce a synergistic effect, thereby fostering more effective suppression of structural distortion than either component alone. The equimolar Ni-304ss composition demonstrates the most stable lattice environment, implying that this binder ratio offers an optimal balance between thermal compatibility and phase stability [35]. In summary, the XRD analysis highlights the crucial role of binder formulation in controlling phase formation, minimizing distortion, and enhancing microstructural coherence in (W,Ti)C-based cermets. The data

support the conclusion that hybrid binders—particularly at a balanced ratio—offer superior performance in stabilizing the ceramic matrix during processing [36].

3.2. Microstructure

Figure 5 shows SEM micrographs of samples with different binder compositions. As seen in Figure 5, cubic carbide grains of the (W,Ti)C hard phase appear in each sample group, while the network-like black phase represents the corresponding binder phase. Furthermore, the microstructure of each sample exhibits the typical bright-core and dark-core microstructural features characteristic of (W,Ti)C-based cemented carbides. The presence of both white and dark core regions within the grains indicates compositional inhomogeneity (or incomplete solid solution) of the (W,Ti)C hard phase. The contrast in SEM images is primarily governed by the atomic number (Z) of the elements. Therefore, the bright cores correspond to W-rich regions (due to the high atomic number of W), typically originating from undissolved WC or W-rich (W,Ti)C particles. Conversely, the dark cores correspond to Ti-rich regions (due to the lower atomic number of Ti), representing undissolved TiC particles. These cores are surrounded by a grey (W,Ti)C-based solid solution rim formed during the liquid phase sintering process. Furthermore, Figure 5 shows that the core rim structure diminishes significantly with increasing 304ss content, indicating that 304ss partially improves the solid solution state of (W,Ti)C and reduces core rim formation. When the binder contained 16 wt.% Ni, the sample exhibited uneven grain distribution with large size variations and numerous bright and dark cores. Adding 4 wt.% 304ss is introduced, the grain distribution improves compared to samples without 304ss, though bright and dark cores remain prevalent. As 304ss content further increases, the grain distribution gradually becomes more uniform, and the number of bright and dark cores decreases. Analysis suggests that during liquid phase sintering, alloying elements from the binder, specifically Cr (introduced by the 304ss), tend to segregate at the hard phase/binder interface. This segregation reduces the interfacial energy and restrains the dissolution-reprecipitation process by inhibiting the migration of W and Ti atoms. Consequently, this effect suppresses excessive grain growth and promotes a more uniform grain size distribution. As the 304ss content increases, the higher concentration of these inhibiting elements (Cr) leads to the observed improvement in microstructural uniformity [37].

Figure 6 shows the grain size distribution histogram of (W,Ti)C cemented carbide with different binder compositions, calculated statistically using grain size analysis software (ImageJ, version 1.52, NIH, Bethesda, MD, USA).

The grain distribution curve and cumulative frequency curve were obtained by fitting with the Gauss function and Boltzmann function, respectively. μg denotes the average grain size, while d50 and d90 represent the particle size indices corresponding to cumulative particle size distributions reaching 50% and 90% for the respective samples. The figure indicates that the sample with 16 wt.% Ni binder exhibits the smallest average grain size, measured at 2.790 ± 0.094 μm. As the Ni content decreased and the 304ss content increased, the average grain size progressively increased, reaching a maximum value of 3.450 ± 0.097 μm at 8 wt.% 304ss-8 wt.% Ni. Subsequently, the average grain size showed no significant change. However, from Figure 6a–e, the grain size distribution rectangles gradually converged toward the center and narrowed. Points with abnormal grain sizes gradually decreased, and the grain size distribution became increasingly uniform. This phenomenon may stem from the poor wettability of Fe with the (W,Ti)C matrix, creating conditions conducive to grain growth [38]. Consequently, increasing 304ss content leads to higher Fe levels and progressively larger grains. However, besides Fe, 304ss also contains alloying elements such as Cr and Mn. The addition of these alloying elements inhibits grain growth, promoting a more uniform grain size distribution. Consequently, after the

304 content reaches 8 wt.%, the average grain size shows no significant change, and the grain size distribution gradually tends toward uniformity [39].

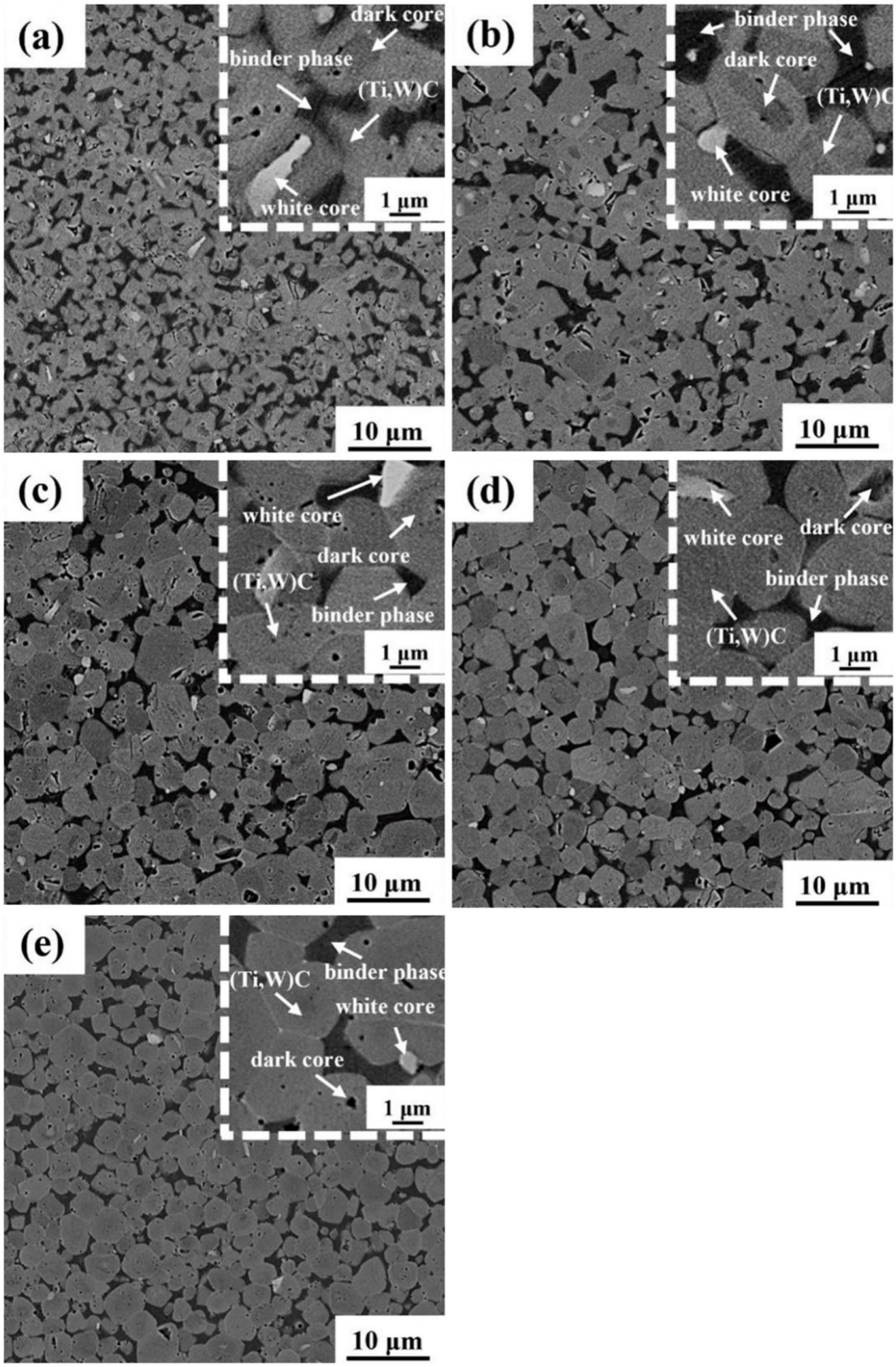

Figure 5. SEM images of samples with different 304ss and Ni content: (**a**) 16Ni-0ss, (**b**) 12Ni-4ss, (**c**) 8Ni-8ss, (**d**) 4Ni-12ss, (**e**) 0Ni-16ss.

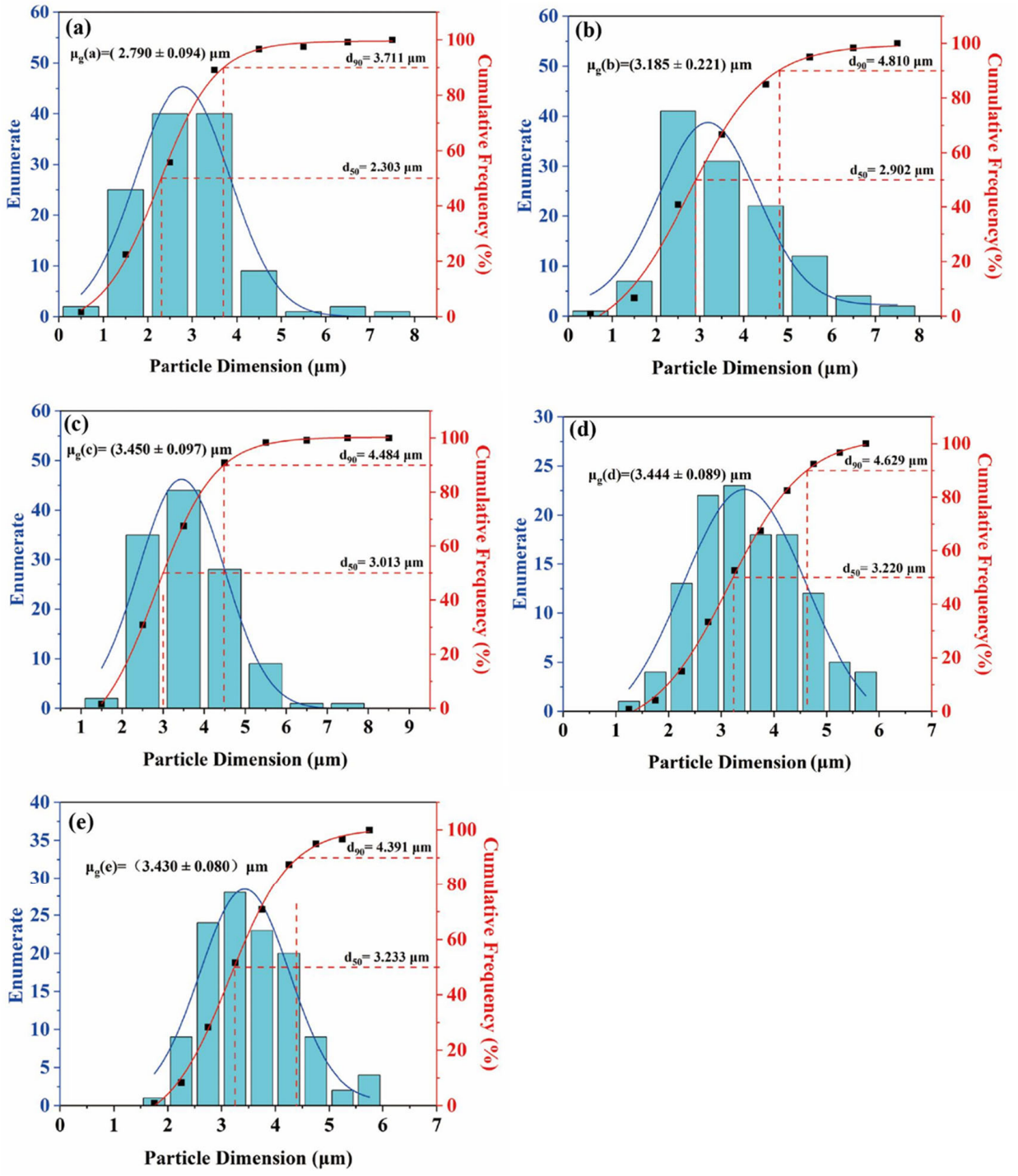

Figure 6. Grain size of samples with different 304ss and Ni contents: (**a**) 16Ni-0ss; (**b**) 12Ni-4ss; (**c**) 8Ni-8ss; (**d**) 4Ni-12ss; (**e**) 0Ni-16ss.

In Sample A3, the optimized grain size and narrowed distribution contribute to a more stable oxide-metal interface, effectively blocking oxygen intrusion.

3.3. Mechanical Properties

Figure 7a presents the variation in density and relative density of the cermets as a function of binder composition. It can be seen that all sintered samples exhibited a high degree of densification, with relative density values exceeding 98%. With the increase of 304ss content, the relative density initially increased, reaching a maximum value of 98.80 ± 0.02% at the binder composition of 8 wt.% 304ss and 8 wt.% Ni. Subsequently,

a slight decline in relative density was observed. Regarding the measured density, a monotonic decrease from 7.530 ± 0.006 g/cm^3 to 7.413 ± 0.003 g/cm^3 was recorded as the 304ss content increased. This trend is consistent with the rule of mixtures, as the theoretical density of 304ss (~7.93 g/cm^3) is lower than that of pure Ni (8.90 g/cm^3). Consequently, the substitution of Ni with the lighter 304ss phase resulted in a reduction in the overall bulk density of the cermets [40].

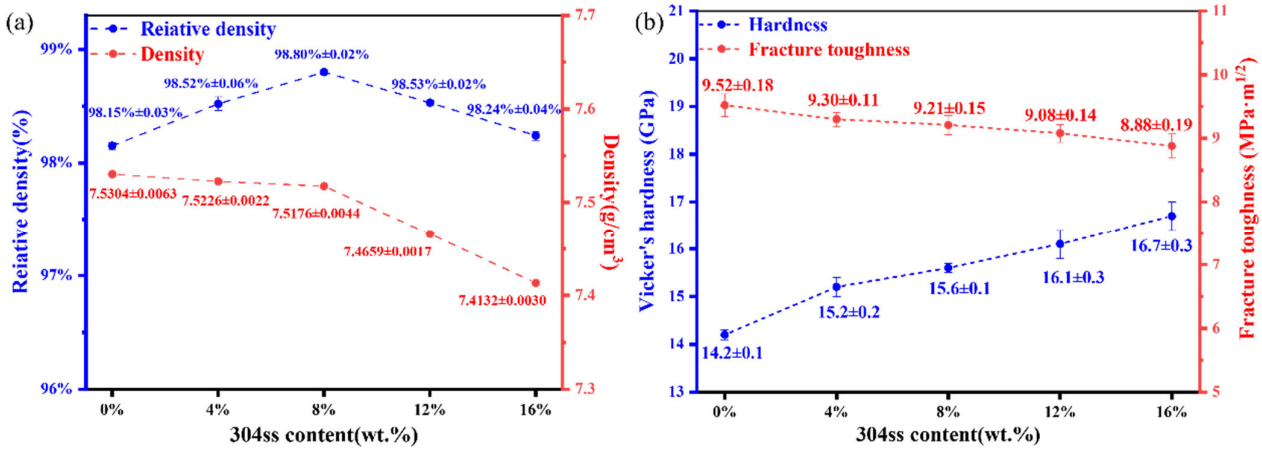

Figure 7. Densification and mechanical properties of the (W,Ti)C-x304ss-(16 − x)Ni (x = 0, 4, 8, 12, 16) samples: (**a**) Density (red line with circles) and relative density (blue line with squares) as a function of 304ss content; (**b**) Vickers hardness (blue line with triangles) and fracture toughness (red line with diamonds) as a function of 304ss content.

Figure 7b illustrates the Vickers hardness and fracture toughness of the samples. The hardness values exhibited a positive correlation with the 304ss content. The sample with pure Ni binder (Sample A1) displayed the lowest hardness of 14.2 ± 0.1 GPa. As the Ni binder was progressively replaced by 304ss, the hardness improved significantly, achieving a peak value of 16.7 ± 0.3 GPa in the sample with pure 304ss binder (Sample A5). This enhancement can be attributed to the intrinsic mechanical properties of the binder phase. The 304 stainless steel possesses a higher yield strength and hardness compared to pure nickel. Furthermore, the alloying elements in 304ss, such as Cr and Mn, contribute to solid solution strengthening within the binder matrix, thereby increasing the resistance of the cermet to plastic deformation [41].

In contrast to hardness, the fracture toughness exhibited an inverse trend. The highest fracture toughness of 9.52 ± 0.18 MPa·m$^{1/2}$ was obtained for the pure Ni-bonded sample, which can be ascribed to the superior ductility of the nickel binder [42]. With the addition of 304ss, the fracture toughness decreased, reaching a minimum in the pure 304ss sample. This trade-off between hardness and toughness is a typical characteristic of cemented carbides. However, the sample with the hybrid binder of 8 wt.% 304ss and 8 wt.% Ni demonstrated an optimal balance of mechanical properties, possessing a high hardness of 15.6 ± 0.1 GPa and a moderate fracture toughness of 9.21 ± 0.15 MPa·m$^{1/2}$. This combination suggests that the hybrid binder system effectively integrates the strengthening effect of 304ss with the toughening effect of Ni [43].

3.4. Oxidation Behavior

Figure 8 illustrates the oxidation behavior of (W,Ti)C-based cermets with different binder compositions at 450 °C. The oxidation rate decreases significantly with the introduction of a Ni-304ss hybrid binder and stabilizes at ~0.023–0.025% for samples A2–A4. In contrast, the cermet with a pure Ni binder (A1) exhibits a higher oxidation rate of 0.0485%. Notably, sample A3 (8 wt.% Ni–8 wt.% 304ss) shows an oxidation rate of 0.0254%,

representing an ~48% reduction compared with the pure Ni binder. It is also found that the cermet containing a pure 304ss binder (A5) displays the highest oxidation rate (0.0517%), despite possessing the highest nominal Cr content. This behavior suggests that Cr-induced passivation alone is insufficient to ensure oxidation resistance when the matrix densification is inadequate. The beneficial effect of Cr can be offset by the increased oxygen transport associated with intrinsic porosity and microstructural defects, as further evidenced by the further corresponding SEM observations [44].

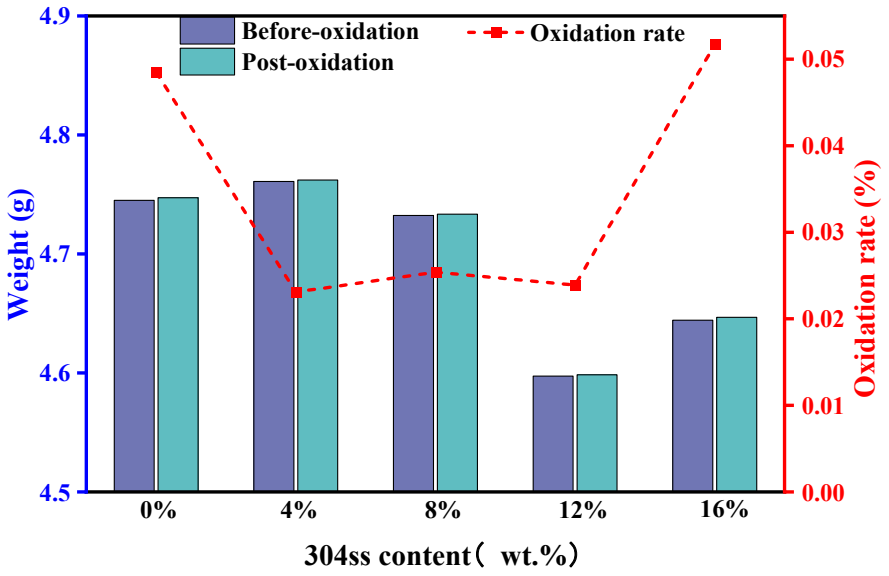

Figure 8. Oxidation weight gain measurements (before and post-oxidation weights) and corresponding oxidation rates for samples A1–A5 at 450 °C.

The surface morphologies of the cermets after isothermal oxidation at 450 °C were examined by SEM, as shown in Figure 9. Compared to the unoxidized specimens, all oxidized cermets were covered by a layer of oxidation products, rendering the originally distinct core-rim structure difficult to discern. For the metal ceramic employing a pure nickel binder (A1, Figure 9a), the oxidized surface was covered by fine granular oxides. This resulted from the differential oxidation rates between the hard phase and the binder phase, presenting a non-uniformly rough surface morphology indicative of direct oxidative erosion of the hard phase [45]. Upon introducing 304 stainless steel into the binder (A2, Figure 9b), the surface oxidation behavior exhibited marked selective differentiation: the greyish-white hard phase particles retained smooth, clean surfaces with no significant oxide accumulation, whereas the binder phase regions originally filling the intergranular voids evolved into a continuous, dark-coloured network structure. This morphological evolution indicates that the oxidation reaction was primarily concentrated within the binder phase regions, while the hard phase skeleton was effectively preserved.

Among all studied compositions, the specimen containing 8 wt% 304 stainless steel (A3, Figure 9c) exhibited excellent structural integrity of the hard phase particles. Unlike the surfaces observed in other groups, the interface between the oxide phase and the hard phase was distinct and dense. The oxidized binder did not peel away but formed a coherent filling within the interstitial voids. This indicates that the oxidation products of the binder successfully blocked diffusion pathways without compromising the structure of the hard phase [46]. However, as the 304 stainless steel content increased further, the sample's oxidation resistance decreased. In the sample with 12 wt.% 304ss (A4, Figure 9d), the contours of hard phase particles became indistinct, with numerous fine oxide nodules scattered across the surface. The dark-coloured binder phase oxidation products no longer

confined themselves to intergranular voids but began to encroach upon portions of the hard phase particle surfaces. The pure 304ss binder sample (A5, Figure 9e) exhibited severe surface damage, including oxide agglomeration and macro-cracks. These observations indicate that excessive stainless steel content compromises the effectiveness of the protective barrier, adversely affecting oxidation resistance [47].

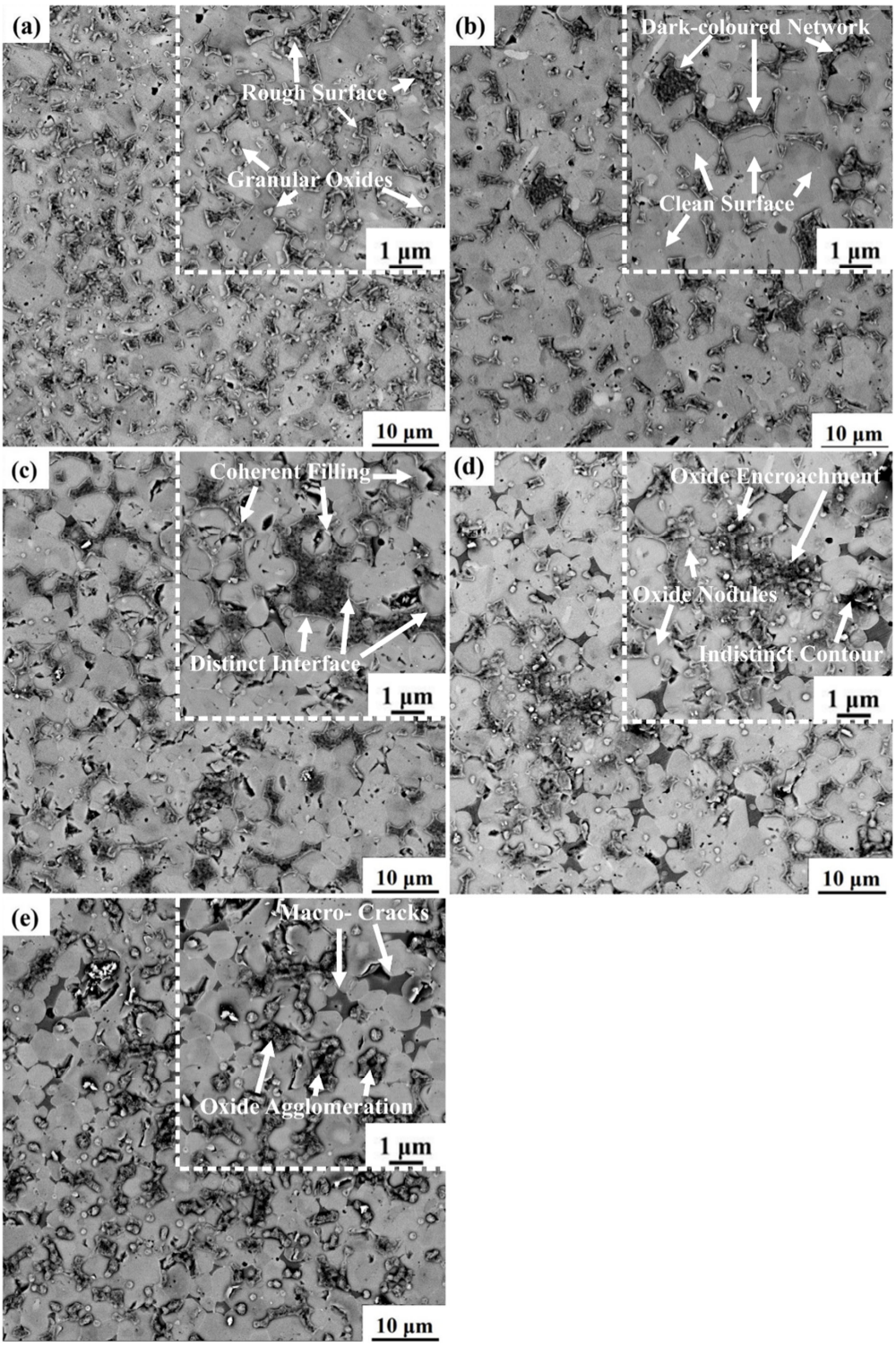

Figure 9. SEM images of oxidized surfaces for cermets (**a**) sample A1, (**b**) sample A2, (**c**) sample A3, (**d**) sample A4, and (**e**) sample A5.

Elemental composition at representative locations of the oxidized specimen C (8 wt.% Ni–8 wt.% 304ss) was analyzed by point EDS, as shown in Figure 10. Points 1 and 3 are enriched in W and Ti, together with a significant oxygen signal, indicating that these regions correspond to the hard phase ((W,Ti)C) and its oxidized derivatives. In contrast, Points 2 and 4 exhibit markedly higher concentrations of Fe and Ni, accompanied by detectable oxygen, and are therefore attributed to the binder phase and its oxidation products. Notably, Point 4 shows the highest oxygen content (58.12%), suggesting more severe oxidation in the binder phase at 450 °C. This observation is consistent with the SEM results, which indicate preferential oxidation of the metallic binder relative to the ceramic hard phase.

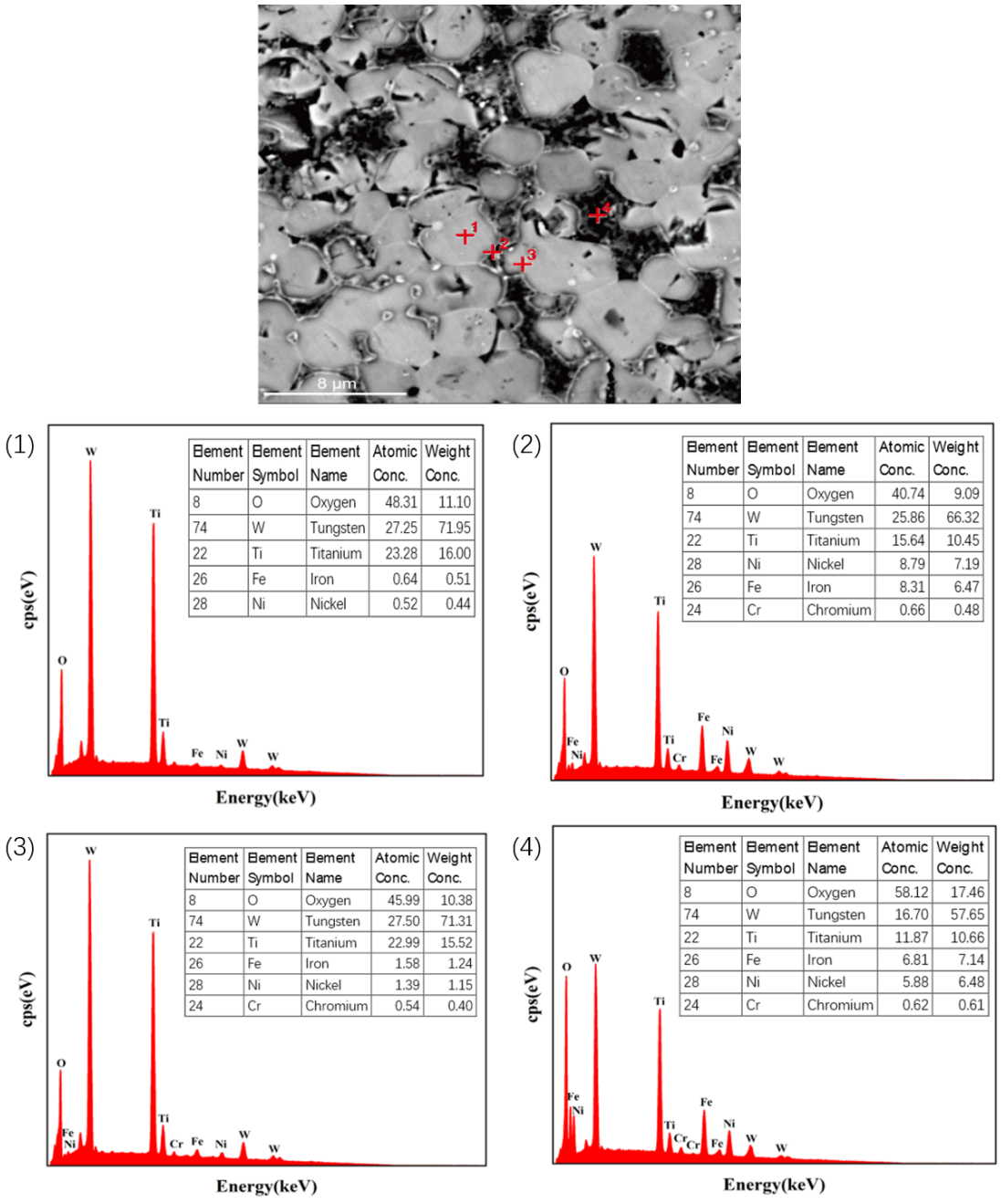

Figure 10. SEM images of sample A3 and the EDS elemental distribution of points 1–4 corresponding to (**1**–**4**).

Chromium is detected at the oxidized binder regions, implying its participation in the oxidation process. The enrichment of Cr near the surface is consistent with the formation

of Cr-containing oxide species that contribute to surface passivation. However, no distinct Cr_2O_3 diffraction peaks are observed in the XRD patterns, which can be attributed to the low concentration and/or amorphous or thin-film nature of the Cr-rich oxides formed during oxidation [45]. Additionally, minor amounts of Ti and W are detected within the binder regions (Points 2 and 4), suggesting partial dissolution or redistribution of these elements into the binder phase during liquid-phase sintering, likely through solid-state or interfacial reactions.

Notably, the absence of a carbon signal in the EDS analysis is attributed to the shielding effect of the surface oxide scale and the limited detection sensitivity of EDS for light elements in a heavy-metal matrix, rather than a total loss of carbon from the substrate [48].

X-ray diffraction was employed to examine the phase constitution of the oxidized cermets, and the corresponding patterns are presented in Figure 11. For all compositions, the diffraction profiles are dominated by the characteristic peaks of the (W,Ti)C hard phase (PDF#03-065-8811), indicating that the ceramic matrix remains structurally stable after oxidation at 450 °C.

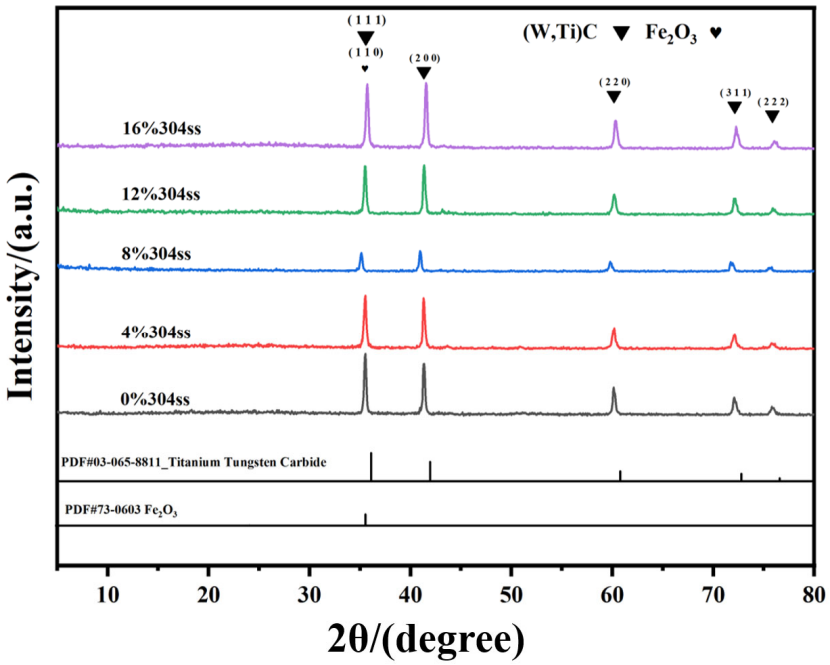

Figure 11. XRD of (W,Ti)C-x304ss-(16 − x)Ni (x = 0, 4, 8, 12, 16%) cermets after oxidation at 450 °C.

In the cermets containing 304 stainless steel, weak additional reflections attributable to Fe_2O_3 (PDF#73-0603) are detected. As indicated by the marked positions, these Fe_2O_3 reflections are of low intensity and partially overlap with the primary (W,Ti)C (111) peak located at approximately $2\theta \approx 36^\circ$, suggesting a limited extent of oxidation of the Fe-containing binder component. Notably, no distinct diffraction peaks corresponding to NiO or Cr_2O_3 are observed for any of the samples. This absence implies that Ni- and Cr-containing oxides, if present, are either below the detection limit of XRD or exist in amorphous or ultra-thin forms. Such behavior is commonly reported for Cr-bearing alloys during early-stage oxidation at low-to-intermediate temperatures, where Cr-rich oxides preferentially form thin, protective layers rather than well-crystallized bulk phases [49].

Figure 12 shows that the oxidation behavior of the (W,Ti)C-based cermets is governed by coupled microstructural and chemical mechanisms. At the microstructural scale, the refined grain structure and reduced porosity achieved in the hybrid Ni-304ss binder compositions effectively suppress rapid oxygen transport along grain boundaries and interconnected pores. The relationship between grain size and oxidation kinetics is significant.

Finer grains provide higher grain boundary density, which facilitates chromium diffusion toward the surface and promotes the formation of a dense, chromium-rich protective oxide layer [50]. In Sample A3, the optimized grain size and narrowed distribution contribute to a more stable oxide-metal interface, effectively blocking oxygen intrusion. From a chemical perspective, Ni promotes interfacial bonding and matrix densification during sintering, thereby limiting the availability of fast diffusion pathways for oxygen ingress [51]. Meanwhile, the presence of Cr in the stainless steel component contributes to oxidation resistance through the formation of Cr-enriched oxide species at or near the surface, which impede further oxygen diffusion. The synergistic interaction between Ni-induced densification and Cr-related surface passivation plays a critical role in maintaining the integrity and continuity of the oxide scale. In contrast, in compositions with unbalanced binder chemistry (pure Ni or pure stainless steel), the absence of either sufficient densification or effective passivation leads to non-protective oxide scales, resulting in the porous or cracked morphologies observed in SEM [52].

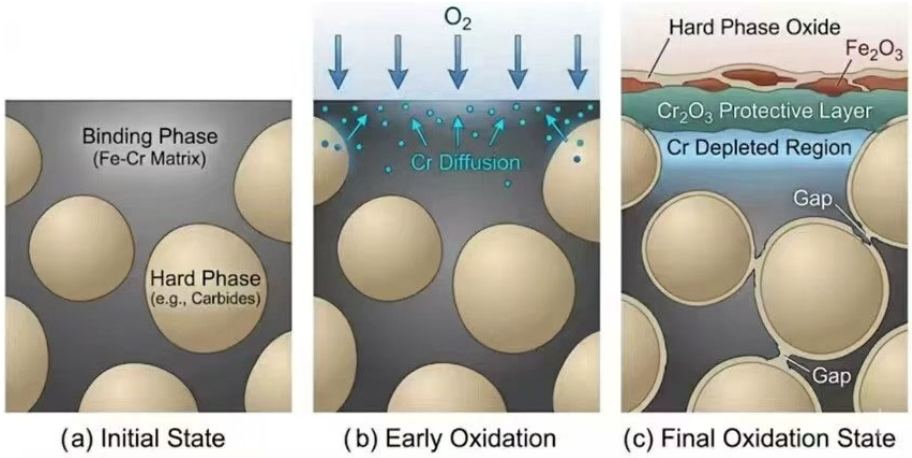

Figure 12. Schematic diagram of the oxidation process.

To further validate the competitive advantages of the developed material, Table 2 compares the properties of the Sample A3 (8% Ni–8% 304 stainless steel) with those of typical WC-Ni, WC-Fe, and Ti(C,N)-based systems reported in the literature [53–56]. The comparison reveals that while Ti(C,N)-based cermets typically exhibit excellent oxidation resistance, their hardness (approximately 12.2 GPa) is often lower than that of WC-based materials. Conversely, WC-Ni and WC-Fe systems achieve high hardness (approximately 15.5 GPa) and toughness but suffer from excessively rapid oxidation rates. Sample A3 (8% Ni–8% 304 stainless steel) effectively bridges this gap. Its hardness reaches 15.6 GPa, comparable to optimized WC-Ni, while maintaining oxidation rates equivalent to Ti(C,N)-based systems. This unique combination demonstrates that the hybrid Ni-304 stainless steel binder successfully integrates nickel's strengthening effect with stainless steel's passivation capability.

Table 2. Sample A3 (8%Ni–8%304ss) compared with other typical cermet systems in mechanical properties and oxidation performance.

System	Hardness (GPa)	Fracture Toughness (K_{IC}, MPa·$m^{1/2}$)	Oxidation Behavior (Qualitative/Rate)
Sample A3 (8%Ni–8%304ss)	15.6 ± 0.1	9.21 ± 0.15	Low (~0.025% mass gain)
WC-Ni System (Optimized)	14.7–15.5	9.5–10.6	High (Porous NiO formation)

Table 2. *Cont.*

System	Hardness (GPa)	Fracture Toughness (K_{IC}, MPa·m$^{1/2}$)	Oxidation Behavior (Qualitative/Rate)
WC-Fe System (FeNiCr binder)	~14.3	~13.7	High (**k**n ≈ 4.57 at 650 °C)
Ti(C,N)-304ss (FeNiCr binder)	~12.2	~11.4	Low (**k**n ≈ 0.13 at 650 °C)

Considering the overall performance trade-off, Sample A3 (8%Ni–8%304ss) is identified as the optimal candidate for industrial wear-resistant applications, offering superior stability compared to pure Ni or pure 304ss binders.

4. Conclusions

This study systematically elucidates the microstructural evolution and property correlations in (W,Ti)C-based Co-free cermets tailored with a Ni-304ss hybrid binder. With the progressive incorporation of 304ss, the lattice distortion of the (W,Ti)C matrix manifests a nonlinear evolutionary trend: at 8 wt.% 304ss, the Ni-Cr synergy minimizes crystallographic strain, whereas excessive 304ss (>8 wt.%) exacerbates distortion due to the combined effects of Fe-induced compromised wetting and grain boundary pinning by Cr and other alloying elements. Microstructural analysis reveals that 304ss incorporation effectively mitigates compositional heterogeneity, suppressing core rim structures and shifting the grain size distribution towards greater uniformity (d50 increasing from 2.79 μm to 3.45 μm). However, the narrowed grain size distribution caused by 304ss addition indicates its bimodal effect on grain growth kinetics.

Mechanical testing demonstrates a linear increase in Vickers hardness from 14.2 to 16.7 GPa with 304ss content, primarily attributed to solid-solution strengthening from Cr and other alloying elements within the binder phase, while fracture toughness decreases from 9.52 to 8.15 MPa·m$^{1/2}$ as Ni content diminishes. The sample A3 (8Ni-8ss) demonstrates a balanced performance of 15.6 GPa hardness and 9.21 MPa·m$^{1/2}$ toughness, confirming that the hybrid binder optimizes strength-toughness compatibility through interfacial reconstruction. Furthermore, the high Vickers hardness and homogeneous microstructure of the Sample A3 suggest superior abrasive wear resistance according to Archard's law.

Oxidation experiments demonstrate that 304ss contents within 4–12 wt.% enable Ni-304ss synergism to form dense Cr_2O_3/NiO composite oxide layers, with oxidation rates maintained at 0.023–0.025%, which is significantly lower than that of the pure Ni system (0.0485%). However, the pure 304ss system exhibits an increased oxidation rate (0.0517%) due to insufficient sintering density (98.3% relative density). XRD and EDS results reveal that the formation of protective Cr_2O_3 layers through Cr enrichment necessitates Ni-induced dense matrix support; otherwise, porosity accelerates the formation of non-protective Fe_2O_3.

The enhanced performance arises from three synergistic mechanisms of the Ni-304ss hybrid binder, Ni-facilitated sintering densification blocking oxygen diffusion pathways, Cr segregation forming passivation layers, and Ni/Cr interdiffusion optimizing intergranular stress compatibility. The 8Ni-8ss system thus represents a critical compositional optimum, offering a theoretical pathway for designing oxidation-resistant Co-free cermets.

Author Contributions: Conceptualization, Y.Z., Y.X., Z.G. and M.Y.; Methodology, Y.Z. and Y.X.; Investigation, Y.Z., Y.X., L.W., X.X., G.X., T.Y., J.C., W.W. and J.D.; Writing—original draft preparation, Y.Z.; Writing—review and editing, Z.G. and M.Y.; Review and editing, Y.Z., Y.X., W.W., J.D., L.W., X.X., G.X., T.Y. and J.C.; Funding acquisition, Z.G. All authors have read and agreed to the published version of the manuscript.

Funding: This research was financially supported by the Sichuan Science and Technology Program (2026YFHZ0152, 2022SZY002Z), Dongfang Electric Corporation-Sichuan University Joint Innovation Research Institute Project [24H1275].

Data Availability Statement: The original contributions presented in this study are included in the article. Further inquiries can be directed toward the corresponding author.

Conflicts of Interest: Authors Wei Wang and Juanqiang Ding were employed by the company Dongfang Electric Corporation Dongfang Turbine Co., LTD. The remaining authors declare that the research was conducted in the absence of any commercial or financial relationships that could be construed as a potential conflict of interest.

References

1. Roebuck, B. World directory and handbook of hardmetals and hard materials. *Surf. Eng.* **1997**, *13*, 27–28. [CrossRef]
2. Upadhyaya, G.S. *Cemented Tungsten Carbides: Production, Properties and Testing*; William Andrew: Norwich, NY, USA, 1998.
3. Seo, J.; Song, J.; Lee, D.; Yang, J.; Choi, I.-H.; Kim, M.; Kwon, H. Effects of adding alloying elements to nickel on the hardening of WC–Ni cemented carbides. *J. Asian Ceram. Soc.* **2025**, *13*, 169–180. [CrossRef]
4. Guo, Z.; Xiong, J.; Yang, M.; Jiang, C. WC–TiC–Ni cemented carbide with enhanced properties. *J. Alloys Compd.* **2008**, *465*, 157–162. [CrossRef]
5. Shichalin, O.; Buravlev, I.Y.; Papynov, E.; Golub, A.; Belov, A.; Buravleva, A.; Sakhnevich, V.; Dvornik, M.; Vlasova, N.; Gerasimenko, A. Comparative study of WC-based hard alloys fabrication via spark plasma sintering using Co, Fe, Ni, Cr, and Ti binders. *Int. J. Refract. Met. Hard Mater.* **2022**, *102*, 105725. [CrossRef]
6. Guo, Z.; Xiong, J.; Yang, M.; Song, X.; Jiang, C. Effect of Mo_2C on the microstructure and properties of WC–TiC–Ni cemented carbide. *Int. J. Refract. Met. Hard Mater.* **2008**, *26*, 601–605. [CrossRef]
7. de Oro Calderon, R.; Agna, A.; Gomes, U.U.; Schubert, W.-D. Phase formation in cemented carbides prepared from WC and stainless steel powder–an experimental study combined with thermodynamic calculations. *Int. J. Refract. Met. Hard Mater.* **2019**, *80*, 225–237. [CrossRef]
8. Aristizabal, M.; Sanchez, J.; Rodriguez, N.; Ibarreta, F.; Martinez, R. Comparison of the oxidation behaviour of WC–Co and WC–Ni–Co–Cr cemented carbides. *Corros. Sci.* **2011**, *53*, 2754–2760. [CrossRef]
9. Heydari, L.; Lietor, P.F.; Corpas-Iglesias, F.A.; Laguna, O.H. Ti (C, N) and WC-based cermets: A review of synthesis, properties and applications in additive manufacturing. *Materials* **2021**, *14*, 6786. [CrossRef]
10. Cai, J.; Wang, Z.; Wang, W.; Ding, J.; Cao, X.; Wang, L.; Xiong, Z.; Xia, X.; Liang, L.; Yang, T. Ternary phase induced microstructure regulation and strengthening in (W, Ti) C-Co cermet materials containing hBN. *Int. J. Refract. Met. Hard Mater.* **2025**, *134*, 107434. [CrossRef]
11. Jing, K.; Guo, Z.; Hua, T.; Xiong, J.; Liao, J.; Liang, L.; Yang, S.; Yi, J.; Zhang, H. Strengthening mechanism of cemented carbide containing Re. *Mater. Sci. Eng. A* **2022**, *838*, 142803. [CrossRef]
12. Fernandes, C.; Vilhena, L.; Pinho, C.; Oliveira, F.; Soares, E.; Sacramento, J.; Senos, A. Mechanical characterization of WC–10 wt.% AISI 304 cemented carbides. *Mater. Sci. Eng. A* **2014**, *618*, 629–636. [CrossRef]
13. Fernandes, C.; Oliveira, F.; Senos, A. Reactive sintering and microstructure development of tungsten carbide-AISI 304 stainless steel cemented carbides. *Mater. Chem. Phys.* **2017**, *193*, 348–355. [CrossRef]
14. Li, J.; Lei, G.; Yu, G.; Cao, X.; Xia, Y.; Yan, S.; Xiao, Q.; Ye, X.-X. Ni-substituted WC cemented carbides with chromium carbide coatings: Enhanced high-temperature oxidation resistance. *Surf. Coat. Technol.* **2025**, *515*, 132631. [CrossRef]
15. Long, J.; Yang, J.; Xu, T.; Zeng, R.; Zhang, R.; Cao, Y.; Yuan, M.; Tan, L.; Cui, Y.; Wei, X. Influences of Cr contents on oxidation behavior of WC-Co-Ni-Cr cemented carbides at 900 °C. *Int. J. Refract. Met. Hard Mater.* **2024**, *118*, 106466. [CrossRef]
16. Chen, C.; Guo, Z.; Li, S.; Xiao, Y.; Chai, B.; Liu, J. Microstructure and properties of WC-17Co cermets prepared using different processing routes. *Ceram. Int.* **2019**, *45*, 9203–9210. [CrossRef]
17. Ying, G.; Gong, H.; Xu, P. Migration Behavior of Tungsten carbide in the dissimilar joints of WC-TiC-Ni/304 stainless steel using robotic MIG welding. In *Transactions on Intelligent Welding Manufacturing: Volume I No. 3 2017*; Springer: Singapore, 2018; pp. 145–163.
18. Wu, K.; Zhang, Z.; Liao, H.; Sun, X.; Yu, L. First principles calculation of interfacial stability, electronic and mechanical properties of WC-304 cemented carbides. *Int. J. Refract. Met. Hard Mater.* **2023**, *117*, 106407. [CrossRef]
19. Maurya, H.S.; Akhtar, F.; Prashanth, K. Load and temperature dependent sliding wear performance of Binder Jet 3D printed stainless-steel bonded cermet. *J. Mater. Res. Technol.* **2025**, *37*, 1199–1212. [CrossRef]
20. He, L.; Gao, Y.; Li, Y.; Liu, Z.; Yuan, W.; Chen, W.; Zhao, S.; Liu, H.; Yan, W. Effect of TiB2/WC addition on the oxidation behavior of Ti (C, N)-304ss cermets during the early oxidation stage. *Corros. Sci.* **2019**, *159*, 108118. [CrossRef]

21. Lee, J.-H.; Park, J.-C.; Park, H.-K. Properties of TiC-Mo 2 C-WC-Ni Cermets by a High-Energy Ball Milling/Spark Plasma Sintering. *Arch. Metall. Mater.* **2023**, *68*, 127–130. [CrossRef]
22. Buravleva, A.A.; Fedorets, A.N.; Vornovskikh, A.A.; Ognev, A.V.; Nepomnyushchaya, V.A.; Sakhnevich, V.N.; Lembikov, A.O.; Kornakova, Z.E.; Kapustina, O.V.; Tarabanova, A.E. Spark plasma sintering of WC-based 10wt.% Co hard alloy: A study of sintering kinetics and solid-phase processes. *Materials* **2022**, *15*, 1091. [CrossRef]
23. Dong, D.; Yang, W.; Xiong, H.; Zhang, L.; Shi, K.; Liao, J. Ti (C, N)-based cermets with fine grains and uniformly dispersed binders: Effect of the Ni–Co based binders. *Ceram. Int.* **2020**, *46*, 6300–6310. [CrossRef]
24. Sirohi, S.; Pandey, S.M.; Świerczyńska, A.; Rogalski, G.; Kumar, N.; Landowski, M.; Fydrych, D.; Pandey, C.J.M. Microstructure and mechanical properties of combined GTAW and SMAW dissimilar welded joints between Inconel 718 and 304L austenitic stainless steel. *Metals* **2022**, *13*, 14. [CrossRef]
25. Shen, Q.; Zhang, Y.; Li, X.; Wang, L.; Nie, C. Enhanced wear resistance and corrosion resistance of 304 austenitic stainless steel by duplex surface treatment. *Steel Res. Int.* **2022**, *93*, 2100689. [CrossRef]
26. Liang, H.; Hou, J.; Jiang, L.; Cao, Z. Microstructure and dry-sliding wear resistance of CoCrFeNiMoTix high entropy alloy coatings produced by laser cladding. *Coatings* **2024**, *14*, 221. [CrossRef]
27. Quinn, G.D.; Bradt, R.C. On the Vickers indentation fracture toughness test. *J. Am. Ceram. Soc.* **2007**, *90*, 673–680. [CrossRef]
28. Zheng, Y.; Liu, W.; Wang, S.; Xiong, W. Effect of carbon content on the microstructure and mechanical properties of Ti (C, N)-based cermets. *Ceram. Int.* **2004**, *30*, 2111–2115. [CrossRef]
29. Muñoz-Ortuño, L.; Soria-Biurrun, T.; Vornberger, A.; Pötschke, J.; Ronkainen, J.; Karhumaa, T.; Sánchez-Moreno, J. Effect of powder characteristics on shrinkage kinetics of WC-Co-Cr Zn-reclaimed submicron powders. *Int. J. Refract. Met. Hard Mater.* **2025**, *136*, 107603. [CrossRef]
30. Rafiaei, S.M.; Bahrami, A.; Shokouhimehr, M. Influence of Ni/Co binders and Mo_2C on the microstructure evolution and mechanical properties of (Ti0. 93W0. 07) C–based cermets. *Ceram. Int.* **2018**, *44*, 17655–17659. [CrossRef]
31. Escribano, J.; García, J.; Alvaredo, P.; Ferrari, B.; Gordo, E.; Sanchez-Herencia, A. FGM stainless steel-Ti (C, N) cermets through colloidal processing. *Int. J. Refract. Met. Hard Mater.* **2015**, *49*, 143–152. [CrossRef]
32. Ye, J.; Yin, Z.; Yuan, J. Enhancement effects of FeCoNiCrMn high-entropy alloy doping on the Ti (C, N)-based cermets: Microstructure and mechanical properties. *Int. J. Refract. Met. Hard Mater.* **2024**, *122*, 106695. [CrossRef]
33. Zhao, L.; Lin, N.; Han, X.; Ma, C.; Wang, Z.; He, Y. Influence of microstructure evolution on mechanical properties, wear resistance and corrosion resistance of Ti (C, N)-based cermet tools with various WC additions. *Met. Mater. Int.* **2021**, *27*, 2773–2781. [CrossRef]
34. Mai, C.; Hu, X.; Zhang, L.; Song, B.; Zheng, X. Numerical simulation and experimental verification of residual stress in the welded joints of weldolet–branch pipe dissimilar steels. *Materials* **2022**, *15*, 1044. [CrossRef] [PubMed]
35. Ding, L.; Deng, X.; Xia, W.; Wang, K.; Zhang, Y.; Zhang, Y.; Shao, X.; Wang, J. Development and external validation of a novel nomogram model for predicting postoperative recurrence-free survival in non-muscle-invasive bladder cancer. *Front. Immunol.* **2022**, *13*, 1070043. [CrossRef] [PubMed]
36. Qin, Y.; Yuan, J.; Zhuang, Y.; Ma, B.; Luo, L.; Wu, Y. Study on effect of high-entropy alloy binder on microstructure and properties of WC cemented carbide doped with rare earth oxide. *Coatings* **2023**, *13*, 273. [CrossRef]
37. Kawakami, M.; Kitamura, K. Segregation of dopants at WC/Co and WC/WC interfaces in solid-state-sintered WC-VC-Cr_3C_2-Co cemented carbides. *Mater. Trans.* **2015**, *56*, 1880–1886. [CrossRef]
38. Han, X.; Lin, N.; Li, A.; Li, J.; Wu, Z.; Wang, Z.; He, Y.; Kang, X.; Ma, C. Microstructure and characterization of (Ti, V, Nb, Ta)(C, N) high-entropy ceramic. *Ceram. Int.* **2021**, *47*, 35105–35110. [CrossRef]
39. Li, G.; Peng, Y.; Yan, L.; Xu, T.; Long, J.; Luo, F. Effects of Cr concentration on the microstructure and properties of WC-Ni cemented carbides. *J. Mater. Res. Technol.* **2020**, *9*, 902–907. [CrossRef]
40. Ehira, M.; Egami, A. Mechanical properties and microstructures of submicron cermets. *Int. J. Refract. Met. Hard Mater.* **1995**, *13*, 313–319. [CrossRef]
41. Santamaria, R.; Salasi, M.; Bakhtiari, S.; Leadbeater, G.; Iannuzzi, M.; Quadir, M.Z. Microstructure and mechanical behaviour of 316L stainless steel produced using sinter-based extrusion additive manufacturing. *J. Mater. Sci.* **2022**, *57*, 9646–9662. [CrossRef]
42. Ghasali, E.; Alizadeh, M.; Ebadzadeh, T. Mechanical and microstructure comparison between microwave and spark plasma sintering of Al–B4C composite. *J. Alloys Compd.* **2016**, *655*, 93–98. [CrossRef]
43. Da Silva, C.M.; Girard, A.; Dufond, M.; Fossard, F.; Andrieux-Ledier, A.; Huc, V.; Loiseau, A. Nickel platinum (Ni_x Pt_{1-x}) nanoalloy monodisperse particles without the core–shell structure by colloidal synthesis. *Nanoscale Adv.* **2020**, *2*, 3882–3889. [CrossRef]
44. Wang, X.; Yang, G.; Chai, Y.; Li, Z.; Che, X.; Wang, Y.; Yang, L.; Zhou, Z. Decreased Preoperative Serum AGR as a Diagnostic Marker of Poor Prognosis after Radical Surgery of Upper Urinary Tract and Bladder Cancers from a Pooled Analysis of 9002 Patients. *Dis. Markers* **2022**, *2022*, 6575605. [CrossRef]

45. Zhu, G.; Liu, Y.; Ye, J. Early high-temperature oxidation behavior of Ti (C, N)-based cermets with multi-component AlCoCrFeNi high-entropy alloy binder. *Int. J. Refract. Met. Hard Mater.* **2014**, *44*, 35–41. [CrossRef]
46. Li, Z.; Liu, X.; Guo, K.; Wang, H.; Dai, P. Microstructure and properties of Ti(C, N)–TiB_2–FeCoCrNiAl high-entropy alloys composite cermets. *Mater. Sci. Eng. A* **2019**, *767*, 138427. [CrossRef]
47. Yi, H.-Q.; Liang, M.-T.; Song, M.; Yin, B.-B.; Qi, F.-G.; Ren, H.-W.; Xie, X.-L.; Yang, Y. A novel corrosion mechanism of Ti (C, N) cermets in molten aluminum induced by high-entropy alloy binders. *Rare Met.* **2025**, *44*, 4119–4136. [CrossRef]
48. Jeor, V.L.S. EDS-Lite, quantitative energy dispersive spectroscopy of light elements. *Microsc. Microanal.* **2017**, *23*, 406–407. [CrossRef]
49. Salman, O.; Gammer, C.; Eckert, J.; Salih, M.; Abdulsalam, E.; Prashanth, K.; Scudino, S. Selective laser melting of 316L stainless steel: Influence of TiB_2 addition on microstructure and mechanical properties. *Mater. Today Commun.* **2019**, *21*, 100615. [CrossRef]
50. Kim, J.-H.; Kim, D.-I.; Suwas, S.; Fleury, E.; Yi, K.-W. Grain-size effects on the high-temperature oxidation of modified 304 austenitic stainless steel. *Oxid. Met.* **2013**, *79*, 239–247. [CrossRef]
51. Li, C.; Zhang, Q.; Wang, F.; Deng, P.; Lu, Q.; Zhang, Y.; Li, S.; Ma, P.; Li, W.; Wang, Y. Microstructure and wear behaviors of WC-Ni coatings fabricated by laser cladding under high frequency micro-vibration. *Appl. Surf. Sci.* **2019**, *485*, 513–519. [CrossRef]
52. Wang, Z.; Du, J.; Su, G.; Sun, Y.; Zhang, C.; Kong, X. Microstructure, preparation and properties of TiC-Fe/FeCoCrNiMn cermet with a core-rim structure. *Vacuum* **2022**, *200*, 110984. [CrossRef]
53. Biedma, Á.; Sánchez, G.; de Nicolás, M.; Bertalan, C.; Useldinger, R.; Llanes, L.; Gordo, E.J.M. A Comparative Study on the Wear Performance and High-Temperature Oxidation of Co-Free Cermets and Hardmetals. *Materials* **2024**, *17*, 3615. [CrossRef]
54. Voitovich, V.; Sverdel, V.; Voitovich, R.; Golovko, E.I. Oxidation of WC-Co, WC-Ni and WC-Co-Ni hard metals in the temperature range 500–800 C. *Int. J. Refract. Met. Hard Mater.* **1996**, *14*, 289–295. [CrossRef]
55. Rocha, A.F.; Bastos, A.; Cardoso, J.; Rodrigues, F.; Fernandes, C.; Soares, E.; Sacramento, J.; Senos, A.; Ferreira, M.J.C.S. Corrosion behaviour of WC hardmetals with nickel-based binders. *Corros. Sci.* **2019**, *147*, 384–393. [CrossRef]
56. Lee, Y.-H.; Ko, S.; Park, H.; Lee, D.; Shin, S.; Jo, I.; Lee, S.-B.; Lee, S.-K.; Kim, Y.; Cho, S. Effect of TiC particle size on high temperature oxidation behavior of TiC reinforced stainless steel. *Appl. Surf. Sci.* **2019**, *480*, 951–955. [CrossRef]

Disclaimer/Publisher's Note: The statements, opinions and data contained in all publications are solely those of the individual author(s) and contributor(s) and not of MDPI and/or the editor(s). MDPI and/or the editor(s) disclaim responsibility for any injury to people or property resulting from any ideas, methods, instructions or products referred to in the content.